Testing quantum fault tolerance on small systems

D. Willsch,[1,2] M. Willsch,[1,2] F. Jin,[1] H. De Raedt,[3] and K. Michielsen[1,2]

[1]*Institute for Advanced Simulation, Jülich Supercomputing Centre, Forschungszentrum Jülich, D-52425 Jülich, Germany*

[2]*RWTH Aachen University, D-52056 Aachen, Germany*

[3]*Zernike Institute for Advanced Materials, University of Groningen, Nijenborgh 4, NL-9747 AG Groningen, The Netherlands*

(Received 15 May 2018; published 28 November 2018)

We extensively test a recent protocol to demonstrate quantum fault tolerance on three systems: (1) a real-time simulation of five spin qubits coupled to an environment with two-level defects, (2) a real-time simulation of transmon quantum computers, and (3) the 16-qubit processor of the IBM Q Experience. In the simulations, the dynamics of the full system is obtained by numerically solving the time-dependent Schrödinger equation. We find that the fault-tolerant scheme provides a systematic way to improve the results when the errors are dominated by the inherent control and measurement errors present in transmon systems. However, the scheme fails to satisfy the criterion for fault tolerance when decoherence effects are dominant.

DOI: 10.1103/PhysRevA.98.052348

I. INTRODUCTION

A functional universal gate-based quantum computer requires a very high level of precision in implementing the quantum gates. In particular when the devices become bigger, it proves difficult to maintain this high level of qubit control [1–5] or to satisfy the requirements needed for a computing device [6]. To overcome these limitations, the most prominent solution is provided by the theory of fault-tolerant quantum computation [7–9].

However, despite many experiments on quantum codes [10–14], it has still remained an open question how much a practical application can profit from a full fault-tolerant protocol. Therefore, Gottesman proposed a test [15] that uses four physical qubits to encode two logical qubits, in combination with a criterion for a successful demonstration of fault tolerance, requiring the following: *All encoded circuits of some representative set perform better than the corresponding bare, unencoded circuits.*

The underlying error-detecting four-qubit code [16–18] has been implemented with ion-trap qubits [19] and on IBM's five-qubit processor [20–22]. Each of these experiments reports a successful result, but none explicitly tests the proposed fault-tolerance criterion.

In this paper, we report on an extensive test of the fault-tolerance criterion for three complementary systems. System (1) consists of five spin qubits coupled to an environment at a given temperature. We consider various weak- and strong-coupling strengths and various temperatures. This system serves as a general model to study decoherence [23–25]. System (2) is an upscaled version of the real-time circuit-Hamiltonian simulation used in [5] comprising five transmons and six resonators. System (3) is the physical 16-qubit device `ibmqx5` provided by IBM [4]. We find very good agreement between the latter two systems for the proper set of optimized gate pulses including measurement errors.

The real-time dynamics of both system (1) and (2) are studied by numerically solving the time-dependent Schrödinger equation (TDSE) with $\hbar = 1$,

$$i\frac{\partial}{\partial t}|\Psi(t)\rangle = H(t)|\Psi(t)\rangle, \tag{1}$$

where $H(t)$ is the time-dependent model Hamiltonian and $|\Psi(t)\rangle$ represents the state of the device at time t. Note that the computer simulation is a deterministic program that always produces the same mathematical solution $|\Psi(t)\rangle$, from which we can compute any physically relevant quantity (such as reduced density matrices of smaller subsystems with nonunitary dynamics) without the need of sampling events. A simulation at this level goes, by definition, beyond perturbative studies, master equations, and assumed Markovianity or completely positive trace-preserving maps [26–28].

We find that despite the goal of quantum error correction, the fault-tolerant scheme fails to satisfy the success criterion under the influence of decoherence errors in system (1). However, our study suggests that fault-tolerant schemes can systematically improve the performance with respect to the natural control and measurement errors dominating the transmon systems (2) and (3).

This paper is structured as follows. In Sec. II, we give a brief overview of the theory of quantum fault tolerance and the protocol that we study. Section III contains the results for system (1). In this system, there are no control errors, allowing us to assess the performance of the fault-tolerant protocol in the presence of decoherence errors only. In Sec. IV, we present the transmon simulation model, i.e., system (2). This system allows us to study the protocol's performance under inherent control and measurement errors. Subsequently, in Sec. V, we present experimental results for system (3). This section also contains a comparison with systems (1) and (2), showing that IBM's transmon qubits are not dominantly affected by decoherence errors and can thus benefit from the fault-tolerant protocol. Finally, conclusions from our study of all three systems are given in Sec. VI.

II. FAULT TOLERANCE

In the framework of quantum fault tolerance, logical qubits are encoded in multiple physical qubits to allow for the detection and correction of errors. This concept inevitably relies on a mathematical model for the errors that are supposed to happen in a physical quantum processor. Simple versions of these models are based on discrete, uncorrelated single-qubit errors or the possibility to describe the errors within the quantum operations formalism [29], while more sophisticated studies consider non-Markovian errors in a general Hamiltonian framework [30–34]. The results of these studies are so-called threshold theorems, stating that as long as a certain parameter in the model is below a certain threshold, arbitrarily long quantum computation is possible.

However, as these threshold theorems are only valid within the mathematical model for the errors, it is unclear whether a particular quantum error-correcting scheme is beneficial in an actual application. For instance, the thresholds are usually expressed in terms of the diamond norm [35], which is experimentally inaccessible. Although progress has been made to relate this quantity to the average gate fidelity [36,37], recent studies have demonstrated that this fidelity, too, cannot be measured in a physical quantum information processor [38]. In fact, it was shown in two independent studies that none of these error metrics can reliably predict the performance of quantum gates in a practical application [5,28].

The fault-tolerant scheme that we test in this study was explicitly designed to apply to small quantum computers [15]. It replaces a bare two-qubit circuit with an encoded four-qubit circuit and an additional ancilla qubit. In this paper, the term *circuit* is defined to include both an initial-state preparation and a sequence of gates. In particular, we consider the initial states $|00\rangle$, $|0+\rangle = |00\rangle + |01\rangle$, and $|\Phi^+\rangle = |00\rangle + |11\rangle$ (up to normalization). In the encoded circuits, these states are represented by entangled four-qubit states (see Appendix A for their definitions and preparation circuits). Along with the encoding of states, there is a set of encoded gates to build a quantum circuit. In the present case, this set is given by $\{X1, X2, Z1, Z2, \text{HHS}, \text{CZ}\}$, where $X1$ and $X2$ denote bit-flip gates, $Z1$ and $Z2$ denote sign-flip gates, HHS denotes the Hadamard gate on each qubit followed by swapping the qubits, and CZ denotes the controlled-phase gate [29]. A full specification of how all bare and encoded circuits are implemented in the fault-tolerant scheme is given in Table III and Table IV in Appendix A.

The aim is to compare the performance of a bare circuit with that of an encoded circuit for a representative set of circuits. To find such a set, we applied the procedure suggested in [15] for the maximum circuit length $T = 10$, the repetition parameter $\text{RP} = 6$, and the periodicity $P = 3$, yielding 465 circuits. In this paper, we focus on the results for a selection of 15 circuits (see Table I) that we consider representative of the performance of all 465 tested circuits (cf. Appendix B).

Evaluating the performance of the circuits is done as follows. For the bare versions, a final measurement of the qubits produces a distribution $p^{\text{bare}}_{q_3q_4}$ of two-bit strings q_3q_4. For the encoded versions, the same measurement produces a distribution of five-bit strings $q_0q_1q_2q_3q_4$. The encoding scheme then dictates that if the ancilla qubit q_0 is 1 or if the bit string $q_1q_2q_3q_4$ includes an odd number of 1's (meaning that it does not correspond to an encoded basis state [15]), it is discarded. The ratio of bit strings that are not discarded is called the *postselection* (PS) ratio r. These selected bit strings then constitute a new distribution $p^{\text{enc}}_{q_3q_4}$, normalized by the PS ratio r. Both bare and encoded distributions can be compared to the theoretical distribution $p^{\text{theory}}_{q_3q_4}$ that an ideal gate-based quantum computer produces. The appropriate measure to compare these distributions is the statistical distance [36],

$$D_{\text{bare}} = \frac{1}{2}\sum_{q_3q_4} \left| p^{\text{bare}}_{q_3q_4} - p^{\text{theory}}_{q_3q_4} \right|, \tag{2}$$

$$D_{\text{enc}} = \frac{1}{2}\sum_{q_3q_4} \left| p^{\text{enc}}_{q_3q_4} - p^{\text{theory}}_{q_3q_4} \right|. \tag{3}$$

In terms of these quantities, Gottesman's success criterion for fault tolerance is fulfilled if $D_{\text{enc}} < D_{\text{bare}}$ for all circuits under investigation.

Mathematical motivations suggesting a better performance of the encoded circuits are (1) the added redundancy in combination with postselection and (2) the fact that an encoded circuit needs two-qubit gates exclusively for the initial-state preparation. However, only practical tests such as the one performed in this paper can tell whether fault-tolerant schemes can improve the performance.

TABLE I. List of the selected 15 circuits to illustrate the difference between bare and encoded versions (see Appendix B for a list of all 465 tested circuits). The first column contains sets of three circuit ID's labeling the circuits in the second column, which consist of particular sets of gates operating on three initial states $|i\rangle \in (|00\rangle, |0+\rangle, |\Phi^+\rangle)$, enumerated in this order.

ID	Circuit
0–2	$\|i\rangle$
240–242	$X1\ X1\ X1\ X1\ X1\ \|i\rangle$
216–218	CZ CZ CZ CZ CZ $\|i\rangle$
171–173	CZ $X1\ X2\ Z1\ Z1\ X1\ X1\ Z1\ Z1\ Z2\ \|i\rangle$
270–272	HHS CZ HHS CZ HHS CZ HHS CZ HHS CZ $\|i\rangle$

III. SPIN QUBITS COUPLED TO AN ENVIRONMENT

System (1) consists of $5 + N_E$ two-level systems. The subsystem with the first five two-level systems represents the spin qubits of the quantum computer, and the remaining N_E two-level systems constitute the environment. This model is motivated by the experimental observation that in recent superconducting quantum processors, two-level systems formed by material defects constitute a major source of decoherence caused by the environment [25,39,40].

We consider the system depicted in Fig. 1. The five qubits have an all-to-all coupling. Each qubit is connected to one two-level system in the environment, which is represented by spins organized on a ring. The Hamiltonian describing the whole system reads

$$H = H_Q + H_E + \lambda H_{QE}, \tag{4}$$

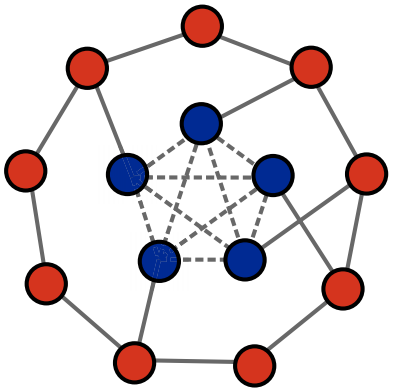

FIG. 1. Schematic representation of the system of five spin qubits (blue) coupled to an environment (red), described by the model Hamiltonian given in Eqs. (4)–(7). The five qubits representing the quantum computer have a tunable all-to-all connectivity (dashed lines). The two-level systems in the environment form a ring with an always-on coupling between nearest neighbors and to the qubits of the quantum computer (solid lines). The latter is controlled by the coupling strength λ.

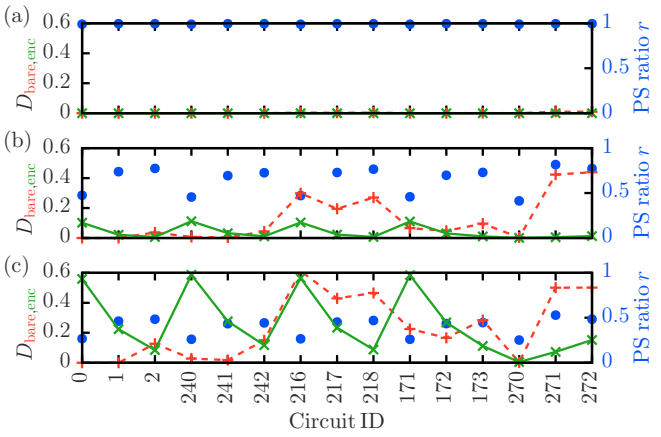

FIG. 2. Test of the fault-tolerance criterion in system (1) for different coupling strengths (a) $\lambda = 0.01$, (b) $\lambda = 0.1$, (c) $\lambda = 0.2$ between the qubits and the environment. Shown are the statistical distances to the ideal result for the selected bare (dashed red line) and encoded (solid green line) circuits as defined in Eqs. (2) and (3), and the postselection ratios (blue dots). All plotted quantities are dimensionless. The simulations were done for inverse temperature $\beta = 1$ and environment $N_E = 20$. Lines connecting the data points are guides to the eye.

where the Hamiltonians H_Q, H_E, and H_{QE} describe the quantum computer, the environment, and the interaction between both, respectively. The parameter λ controls the coupling strength between the quantum computer and the environment. The Hamiltonians H_Q, H_E, and H_{QE} given in Eq. (4) read

$$H_Q = -\sum_{n=0}^{4}\sum_{\alpha=x,z} h_n^\alpha \sigma_n^\alpha - \sum_{n,m=0}^{4} G_{nm}^x \sigma_n^x \sigma_m^x, \tag{5}$$

$$H_E = -\sum_{n=5}^{N_E+4}\sum_{\alpha=x,y,z} J_n^\alpha \sigma_n^\alpha \sigma_{n+1}^\alpha, \tag{6}$$

$$H_{QE} = -\sum_{n=0}^{4}\sum_{\alpha=x,y,z} K_{nj_n}^\alpha \sigma_n^\alpha \sigma_{j_n}^\alpha, \tag{7}$$

where σ_n^α for $\alpha = x, y, z$ denote the Pauli matrices for qubit n. Each qubit $n \in \{0, \ldots, 4\}$ is connected to a randomly chosen qubit $j_n \in \{5, \ldots, N_E + 4\}$ in the environment (all j_n are different) with a random coupling strength $\lambda|K_{nj_n}^\alpha| \approx \lambda \times 2\,\text{GHz}$, tunable through the parameter λ. In the environment Hamiltonian H_E, the couplings J_n^α are chosen randomly from $[-J, J]$ for $J = 2\,\text{GHz}$.

Implementing the quantum gates through piecewise constant parameters in Eq. (5) eliminates any control and measurement errors. Therefore, with this implementation, we can exclusively study the effect of decoherence errors because the only source of errors is the interaction between the qubits and the environment. The comparison with the results of systems (2) and (3) then allows us to understand the difference between decoherence errors and control or measurement errors when using a fault-tolerant protocol. In Appendix C 1, we give the full specification of the parameters h_n^α and G_{nm}^x that enter in H_Q [see Eq. (5)]. In the absence of coupling to the environment, the whole system evolves in time like an ideal quantum computer. Running all quantum circuits on both system (1) for $\lambda = 0$ and the Jülich universal quantum computer simulator [41] yields identical results, validating the correct implementation of the quantum gates.

We solve the TDSE given in Eq. (1) with the piecewise time-independent Hamiltonian given in Eqs. (4)–(7) to machine precision by means of the Chebyshev polynomial representation of $\exp(-itH)$ [42–44]. The environment is prepared at an inverse temperature β using the random-state technology [44,45].

To understand how λ affects the qubit coherence, we estimate the decoherence time T_2 by preparing the qubit along the positive x axis, evolving it in the presence of the environment, and fitting a damped oscillation to the decay of its projection on the x axis; see [46] for more details on this procedure. These experiments are performed at inverse temperature $\beta = 0$ to produce the worst-case decoherence times. We find that $T_2^\lambda \approx 3.7\,\text{ns}/\lambda^2$ (data not shown) and, specifically, $T_2^{\lambda=0.1} \approx 370\,\text{ns}$ and $T_2^{\lambda=0.01} \approx 4\times10^4\,\text{ns}$. In particular, the decoherence time $T_2^{\lambda=0.01}$ is much larger than the time needed to execute a quantum circuit in this model (cf. Table VI in Appendix C 1), which supports the interpretation of $\lambda = 0.01$ representing a very weak coupling between the ideal quantum computer and the environment.

In Fig. 2, we present results for the statistical distances D_{bare} and D_{enc} [see Eqs. (2) and (3)] and the PS ratio r for the circuits listed in Table I. The three cases shown in Figs. 2(a)–2(c) are representative of the transition from very weak coupling $\lambda = 0.01$ to strong coupling $\lambda = 0.2$ between the qubits and the environment. For the weakest coupling [see Fig. 2(a)], the statistical distances for both bare and encoded circuits are nearly zero, and the postselection ratios $r \approx 1$. This shows that in this case, both bare and encoded versions perform almost perfectly [i.e., both produce the ideal result used in Eqs. (2) and (3)]. This observation also

TABLE II. Percentage P of the circuits from Table I for which the encoded version performs better than the bare version, as a function of the coupling strength λ between the qubits and the environment. The coupling strengths range from very weak to strong coupling. The simulations were done for inverse temperature $\beta = 1$ and environment size $N_E = 20$.

λ	0.01	0.025	0.05	0.075	0.1	0.125	0.15	0.175	0.2
P	80%	87%	73%	73%	67%	67%	53%	53%	53%

demonstrates the correct implementation of the quantum computer by means of the model defined by Eqs. (4)–(7).

Increasing the coupling strength λ leads to a stronger influence of decoherence errors on the operation of the quantum computer. Accordingly, in Figs. 2(b) and 2(c), it can be seen that the statistical distances of both bare and encoded circuits increase. Interestingly, one can always find circuits for which the bare version outperforms the encoded version. In particular, every third circuit starting from circuit ID 0 shows a strong increase in D_{enc}. These circuits correspond to the encoding of the state $|00\rangle$. The physical reason behind the sensitivity of these circuits is that the encoding circuit for $|00\rangle$ includes the largest number of two-qubit gates (see Table III in Appendix A). These two-qubit gates typically take a longer time to execute than single-qubit gates [12,19,47] (see also Table VI in Appendix C 1). Hence, the entangling two-qubit gate is the most sensitive gate even when no control errors, but only decoherence errors, are present. The only exception is the circuit with ID 270, which always yields $D_{\text{bare}} \approx D_{\text{enc}} \approx 0$ (see Fig. 2). The reason is that the execution time of this circuit is so long that the interaction with the environment leads to a uniform distribution of all five-qubit states in the quantum computer, which accidentally matches the ideal output distribution (cf. Table I).

A summary of the performance for various intermediate coupling strengths $\lambda \in [0.01, 0.2]$ is given in Table II. Interestingly, the percentage P of encoded circuits performing better than the bare circuits is not a monotonous function of λ. For instance, the largest value of P is found at $\lambda = 0.025$ instead of $\lambda = 0.01$. However, for such a weak coupling, both bare and encoded circuits perform nearly perfectly [cf. Fig. 2(a)].

In addition to the results shown in Fig. 2 and Table II, we have studied the performance of the circuits for different environment sizes $N_E \in \{5, 20, 27\}$ (see Fig. 9 in Appendix C 1) and inverse temperatures $\beta \in \{0, 1, 5\}$ (see Fig. 10 in Appendix C 1), each of which yields results with the characteristic features resembling those in Fig. 2(b). This means that in all analyzed regimes, there are always some encoded circuits that perform worse than their bare equivalents. In other words, we did not find any case that passes the fault-tolerance test.

One may ask whether this result violates the threshold theorems proven in [30–33], which obviously consider a Hamiltonian similar to Eqs. (4)–(7). The answer is that in the threshold theorems, the required value of λ is still orders-of-magnitude smaller than the ones we studied. Yet, already for $\lambda = 0.01$ [see Fig. 2(a)], both bare and encoded circuits perform almost perfectly and encoding still makes the result worse in some cases. We conclude that using a fault-tolerant protocol such as the one suggested in [15] to overcome errors in a system dominated by decoherence errors from two-level defects is not necessarily helpful.

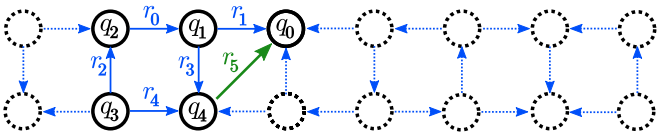

FIG. 3. Schematic image showing the five transmon qubits and six resonators described by the Hamiltonian given in Eqs. (8)–(10). The system represents a subset of the 16-qubit device `ibmqx5` [4] with an additional resonator r_5 to enable the implementation of all bare and encoded circuits. Without this resonator, the encoded circuits with initial state $|00\rangle$ cannot be fault-tolerantly implemented [15].

IV. TRANSMON SIMULATION

System (2) is defined by the circuit Hamiltonian for $N_{\text{tr}} = 5$ superconducting transmon qubits coupled by $N_{\text{res}} = 6$ transmission-line resonators [48,49], a system that can be used to model IBM's publicly accessible quantum processors [4,5]. The simulated system is schematically shown in Fig. 3 as a subset of the 16-qubit device `ibmqx5` [4].

The full Hamiltonian used in the transmon simulation reads

$$H = H_{\text{tr}} + H_{\text{res}}, \tag{8}$$

$$H_{\text{tr}} = \sum_i \{4E_{Ci}[\hat{n}_i - n_{gi}(t)]^2 - E_{Ji}\cos\hat{\varphi}_i\}, \tag{9}$$

$$H_{\text{res}} = \sum_r \Omega_r \hat{a}_r^\dagger \hat{a}_r + \sum_{r,i} G_{ri}\hat{n}_i(\hat{a}_r + \hat{a}_r^\dagger), \tag{10}$$

where $i = 0, \ldots, N_{\text{tr}} - 1$ enumerates the transmon qubits with capacitive energies E_{Ci}, Josephson energies E_{Ji}, number operators $\hat{n}_i$, and superconducting phase operators $\hat{\varphi}_i$. The resonators are labeled by $r = 0, \ldots, N_{\text{res}} - 1$ and are described by their raising and lowering operators $\hat{a}_r^\dagger$ and $\hat{a}_r$, respectively. Their frequencies are given by Ω_r and the capacitive coupling strength between transmon i and resonator r is denoted by G_{ri}. Quantum gates on the transmons are implemented through microwave voltage pulses represented by $n_{gi}(t)$ [5]. A specification of all device parameters and pulse shapes is given in Appendix C 2.

We simulate the transmon computer model defined in Eqs. (8)–(10) by solving the TDSE given in Eq. (1) with the time-dependent Hamiltonian in Eq. (8) using a second-order Suzuki-Trotter product-formula algorithm [5,50,51] with time step $\tau = 0.001$ ns. The simulation includes as many higher levels in the transmons and the resonators as necessary to describe the dynamics of the system accurately (see Appendix C 2 for more information). The device parameters in Eqs. (8)–(10) and optimized gate pulses $n_{gi}(t)$ are chosen such that they represent a subset of five transmons and five resonators from the 16-qubit device `ibmqx5` [4,47,52]. Additionally, a sixth resonator r_5 is included in the model (see Fig. 3) to extend the connectivity such that all circuits of the fault-tolerant scheme

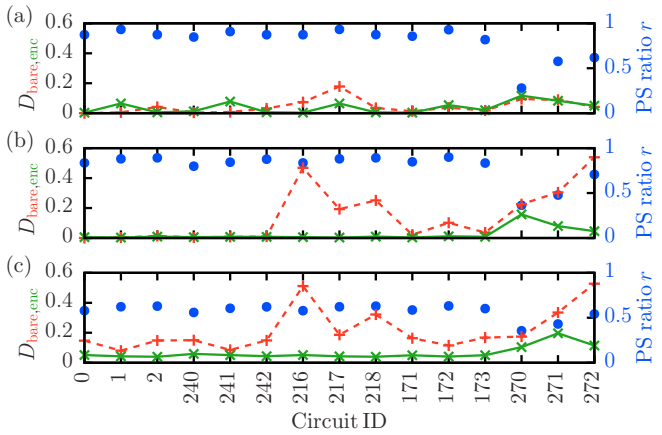

FIG. 4. Test of the fault-tolerance criterion in system (2), i.e., the real-time transmon simulation for different optimized gate sets (a) without frequency tuning, (b) with frequency tuning, and (c) with frequency tuning and measurement error $p = 0.08$. Shown are the statistical distances to the ideal result for the selected bare (dashed red line) and encoded (solid green line) circuits as defined in Eqs. (2) and (3), and the postselection ratios (blue dots). All plotted quantities are dimensionless. Lines connecting the data points are guides to the eye.

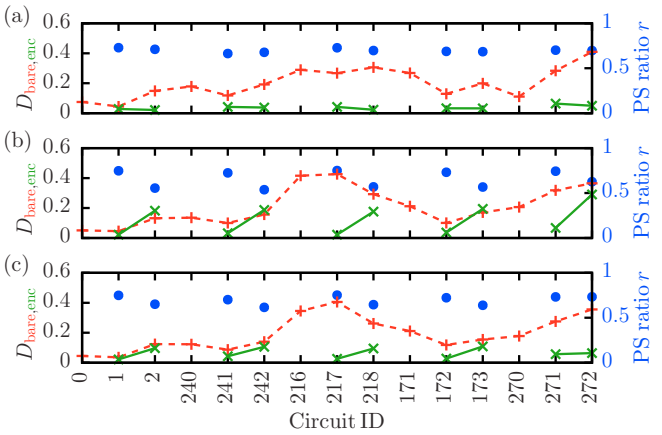

FIG. 5. Test of the fault-tolerance criterion in system (3), i.e., the 16-qubit device `ibmqx5` using the qubits (Q_4, Q_3, Q_2, Q_{15}, Q_{14}) on (a) April 3, 2018, (b) April 9, 2018, and (c) April 19, 2018. Shown are the statistical distances to the ideal result for the selected bare (dashed red line) and encoded (solid green line) circuits as defined in Eqs. (2) and (3), and the postselection ratios (blue dots). All plotted quantities are dimensionless. Only the circuits that could be mapped on the topology were run on the real device. Lines connecting the data points are guides to the eye.

can be implemented. The additional resonator solves the problem faced in [20], where the original fault-tolerant encoding could not be implemented and an alternative encoding was used which, although fault-tolerant in theory, did not pass the fault-tolerance test on the IBM device.

The results of the fault-tolerance test are shown in Fig. 4 for two different gate sets. Both gate sets use Gaussian microwave pulses driven at a certain drive frequency f to implement the quantum gates [see Eq. (C1), Table IX, and Table X in Appendix C 2 for the individual parameters resulting from the pulse optimization]. For the first gate set, this drive frequency was set to the respective qubit frequency for each qubit. As can be seen in Fig. 4(a), the performance is equally good for both bare and encoded circuits. The fault-tolerance criterion $D_{\text{enc}} < D_{\text{bare}}$ is not satisfied.

The second gate set has been obtained by additionally optimizing the drive frequencies of the microwave pulses. This means that the drive frequencies are slightly detuned from the qubit frequencies such that the gate fidelities are slightly better on average (compare [53] and Table XI in Appendix C 2; note, however, that better fidelities do not always imply better gates [5]). Unlike the first gate set, the second gate set shows nearly perfect performance for all the encoded circuits [see Fig. 4(b)], suggesting that a fault-tolerant implementation can profit more from reduced control errors than a bare implementation. In particular, by examining the numerical results used for Fig. 4(b), we find that the fault-tolerance criterion is satisfied for all circuits but the one with ID 0 (corresponding to $|00\rangle$; see Table I). This is the only circuit for which the bare version does not require any pulses and, obviously, applying no pulse is bound to perform better than applying the preparation pulses to encode $|00\rangle$. Therefore, in the absence of additional measurement errors, this exception is reasonable.

To assess the effect expected due to measurement errors, we model an additional error for each qubit such that with probability p, a measured bit 0 is erroneously counted as 1, and vice versa. As shown in Fig. 4(c) for the case $p = 0.08$, the fault-tolerance test is passed for all circuits. Thus, in addition to the natural unitary errors inherently included in the real-time transmon simulation (cf. [5]), the presence of measurement errors is essential to fulfill the fault-tolerance criterion.

V. PHYSICAL TRANSMON DEVICE

System (3) is used to test the fault-tolerance criterion by utilizing the 16-qubit device `ibmqx5` provided by IBM [4]. Using the qubit mapping $q_0q_1q_2q_3q_4 \mapsto Q_4Q_3Q_2Q_{15}Q_{14}$, this device provides the correct connectivity to run all circuits except for the encoded version of the circuits with initial state $|00\rangle$ [a problem which was solved in system (2) by including the additional resonator r_5; see Fig. 3].

The results for 15 out of the 465 tested circuits are shown in Fig. 5 for three different calibrations. We observe that the performance of the device varies for different calibrations. For instance, the experiment on April 9, 2018 shown in Fig. 5(b) failed the fault-tolerance test. However, in general, many runs passed the test for all circuits (see also Fig. 6 in Appendix B for the full set of circuits).

As system (2), discussed in Sec. IV, was designed to simulate a transmon processor such as `ibmqx5`, it is of course tempting to set the results in relation to the experimental observations presented in Fig. 5. The first set of gate pulses used for Fig. 4(a), where the drive frequencies were not optimized but set to the qubit frequencies, shows a circuit performance that differs from the results shown in Fig. 5. In particular, the fault-tolerance test fails. However, the second gate set used for Fig. 4(b) yields a positive result for all circuits

that often passed the test on `ibmqx5` [see Figs. 5(a) and 5(c)]. This suggests that the pulses used on IBM's processor also utilize slightly detuned drive frequencies.

Note that the individual circuit performance of system (3) depends a lot on the pulse parameters found in the calibration procedure. For instance, in Figs. 5(b) and 5(c), the encoded circuits with initial state $|\Phi^+\rangle$ always perform slightly worse than the encoded circuits with initial state $|0+\rangle$. We examined the gate errors reported by IBM for the corresponding two-qubit gates, finding that they reflect this observation on April 9 and April 19. The reason that we cannot observe this feature in Fig. 4 for system (2) is that our pulse-optimization procedure produces slightly more reliable pulse parameters whose two-qubit error rates do not spread as much and also do not differ between runs on separate days (cf. Table XI in Appendix C 2).

The best agreement between simulation and experiment is achieved when an additional measurement error is taken into account [see Fig. 4(c)]. In particular, the fault-tolerance criterion is then also satisfied for every encoded circuit that could not be run on `ibmqx5` (corresponding to the circuit IDs 0, 240, 216, 171, and 270). This suggests that the positive result for the fault-tolerance test may also be observed if the device's connectivity is extended to support the complete set of circuits, as was done in the simulation (see Fig. 3).

A direct comparison to system (1), i.e., the system of spin qubits coupled to an environment discussed in Sec. III, yields another interesting conclusion. Clearly, the performance of the tested circuits shown in Fig. 2 differs largely from the results shown in Fig. 5 in that the fault-tolerance criterion for system (1) was not satisfied for any of the studied set of parameters. This led to the conclusion that decoherence errors are difficult to mitigate with the fault-tolerant scheme. However, Figs. 5 and 6 (see Appendix B) show that the fault-tolerance criterion can indeed be achieved in the IBM Q Experience. Thus we conclude that the errors in IBM's quantum processors are not dominated by decoherence from material defects.

VI. DISCUSSION

We have tested a full fault-tolerant protocol encoding two logical qubits on three complementary systems, each dominated by a certain type of errors present in applications. Since these errors can be much more complicated than those assumed in the design of fault-tolerant protocols, it is by no means guaranteed that using a fault-tolerant protocol improves the computation.

System (1) is a set of five spin qubits coupled to an environment with various coupling strengths, sizes, and temperatures. This system suffers only from decoherence errors that are controlled by the coupling strength. We found that the fault-tolerance criterion is not satisfied for any set of parameters, suggesting that dominating decoherence errors are hard to mitigate with a fault-tolerant scheme.

System (2) is a model system of five transmon qubits and six resonators, in which the quantum gates are implemented by the same Gaussian microwave pulses that are also used in experiments [5,47,52,54]. Lacking an environment, this system's performance is purely affected by unitary control errors. We found that for the appropriate set of gate pulses with detuned drive frequencies, a full fault-tolerant protocol can systematically improve a quantum computer's performance. In the presence of an additional measurement error, we showed that the fault-tolerance criterion is satisfied for all circuits under investigation.

System (3) is a physical implementation of a quantum computer based on transmon qubits, namely, the device `ibmqx5` of the IBM Q Experience [4]. While the results varied with the day on which we carried out the experiments, the general observation was that the fault-tolerance criterion is satisfied for all circuits that could be mapped on the device topology. Furthermore, by comparing the experimental results with the simulation results for system (2), we found that this observation still holds if the device's topology is extended to support the complete set of circuits. A comparison with the results for system (1) further suggests that the errors in IBM's quantum processor are largely control and measurement errors, implying that the device is well isolated from decoherence due to material defects.

Based on these results, we conclude that the performance of a quantum computer can be systematically improved with a fault-tolerant protocol, as long as the errors of the underlying processor are due to control and measurement errors. However, the use of a fault-tolerant scheme is not necessarily helpful when decoherence errors are dominant.

ACKNOWLEDGMENTS

We acknowledge use of the IBM Q Experience for this work. The views expressed are those of the authors and do not reflect the official policy or position of IBM or the IBM Q Experience team. D.W. is supported by the Initiative and Networking Fund of the Helmholtz Association through the Strategic Future Field of Research project "Scalable solid state quantum computing (ZT-0013)." The authors acknowledge the computing time granted by the JARA-HPC Vergabegremium and provided on the JARA-HPC Partition part of the supercomputer JUQUEEN [55] at the Forschungszentrum Jülich.

APPENDIX A: SPECIFICATION OF THE FAULT-TOLERANT SCHEME

The error-detecting code used in the fault-tolerant scheme is the [[4,2,2]] code, where the logical two-qubit states are defined as

$$\overline{|00\rangle} = (|0000\rangle + |1111\rangle)/\sqrt{2}, \tag{A1}$$

$$\overline{|01\rangle} = (|1100\rangle + |0011\rangle)/\sqrt{2}, \tag{A2}$$

$$\overline{|10\rangle} = (|1010\rangle + |0101\rangle)/\sqrt{2}, \tag{A3}$$

$$\overline{|11\rangle} = (|0110\rangle + |1001\rangle)/\sqrt{2}. \tag{A4}$$

By linear combination, one can derive the encoded versions of the other two initial states considered in this study,

$$\overline{|0+\rangle} = (|0000\rangle + |1100\rangle + |0011\rangle + |1111\rangle)/2, \tag{A5}$$

$$\overline{|\Phi^+\rangle} = (|0000\rangle + |0110\rangle + |1001\rangle + |1111\rangle)/2. \tag{A6}$$

TABLE III. Initial states and the bare and encoded versions of their preparation circuits.

State	Bare version	Encoded version
$\|00\rangle$	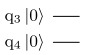	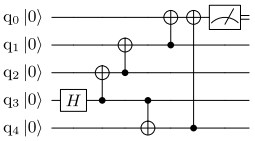
$\|0+\rangle$	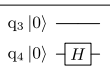	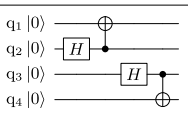
$\|\Phi^+\rangle$	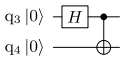	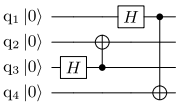

The physical four-qubit states are enumerated in increasing order as $q_1q_2q_3q_4$ and an additional qubit q_0 is used as the ancilla qubit. Using this labeling, the logical gates used in the tested circuits map to the physical gates according to

$$\overline{\mathrm{X1}} = X_1X_3, \tag{A7}$$

$$\overline{\mathrm{X2}} = X_1X_2, \tag{A8}$$

$$\overline{\mathrm{Z1}} = Z_1Z_2, \tag{A9}$$

$$\overline{\mathrm{Z2}} = Z_1Z_3, \tag{A10}$$

$$\overline{\mathrm{HHS}} = H_1H_2H_3H_4, \tag{A11}$$

$$\overline{\mathrm{CZ}} = S_1S_2S_3S_4Z_2Z_3, \tag{A12}$$

which can be easily verified by applying the logical gates to the definition of the logical states given in Eqs. (A1)–(A4). In Table III and Table IV, we give a specification of all gate sequences used to assemble the bare and encoded versions of the circuits to test the fault-tolerance criterion.

APPENDIX B: FULL SET OF TESTED CIRCUITS

In Table V, we give a list of all 465 circuits generated by the procedure suggested in [15] for the maximum circuit length $T = 10$, the repetition parameter $\mathrm{RP} = 6$, and the periodicity $P = 3$.

TABLE IV. Bare and encoded gate elements.

Gate	Bare version	Encoded version
X1		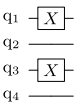
X2		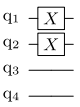
Z1		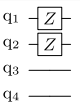
Z2		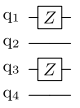
HHS	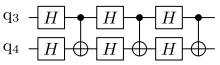	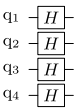
CZ	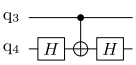	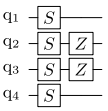

A representative result of the performance of all circuits on the IBM device is shown in Fig. 6 [note that the interruptions in the solid green line are due to the fact that the encoded version of $|00\rangle$ cannot be prepared using the topology of system (3)]. This result undeniably demonstrates that encoding the circuits according to the fault-tolerant scheme can improve the overall performance of the circuits that can be implemented on the device. However, as already mentioned in Sec. V, the fault-tolerance criterion was not satisfied on all days that we ran the experiment. One such result is shown in Fig. 7 where some of the encoded circuits with initial state $|\Phi^+\rangle$ have rather high statistical distances and low PS ratios.

For completeness, we also present results for the full set of circuits tested in the decoherence model [system (1)] in Fig. 8. This figure does not have the above-mentioned interruptions since, in system (1), all 465 circuits can be implemented and tested in both their bare and encoded version.

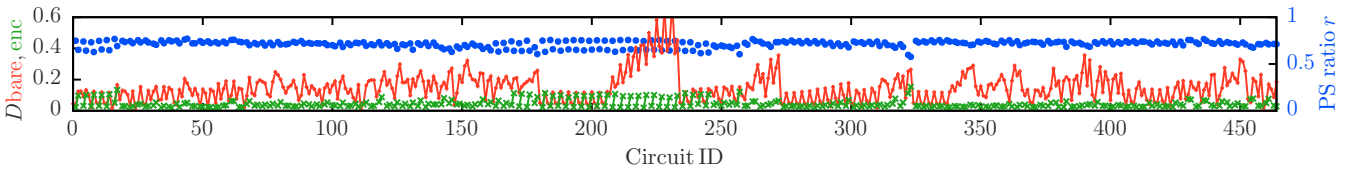

FIG. 6. Test of the fault-tolerance criterion in system (3) (see Sec. V) for all 465 circuits using the qubits (Q_4, Q_3, Q_2, Q_{15}, Q_{14}) of the IBM 16-qubit device `ibmqx5` on April 19, 2018. Shown are the statistical distances to the ideal result for the selected bare (red plusses) and encoded (green crosses) circuits, and the postselection ratios (blue dots). All plotted quantities are dimensionless. Only the circuits that could be mapped on the topology were run on the real device. Lines connecting the data points are guides to the eye.

TABLE V. List of all 465 circuits used to test the fault-tolerance criterion. The elements consist of a range of three circuit IDs labeling the subsequent circuits, which consist of a particular set of gates operating on three initial states $|i\rangle \in (|00\rangle, |0+\rangle, |\Phi^+\rangle)$, enumerated in this order.

0-2 |i⟩
3-5 X1 |i⟩
6-8 X2 |i⟩
9-11 Z1 |i⟩
12-14 Z2 |i⟩
15-17 HHS |i⟩
18-20 CZ |i⟩
21-23 X2 Z1 |i⟩
24-26 HHS Z1 |i⟩
27-29 Z1 Z2 |i⟩
30-32 X1 HHS |i⟩
33-35 CZ Z2 |i⟩
36-38 Z2 Z1 CZ |i⟩
39-41 Z1 X2 X2 |i⟩
42-44 CZ CZ HHS |i⟩
45-47 X1 X1 X1 |i⟩
48-50 Z2 X2 Z1 |i⟩
51-53 X1 X2 X1 |i⟩
54-56 X2 X1 CZ X1 |i⟩
57-59 HHS Z2 CZ Z1 |i⟩
60-62 HHS X1 Z2 Z2 |i⟩
63-65 CZ Z2 Z1 Z2 |i⟩
66-68 HHS HHS HHS Z1 |i⟩
69-71 X2 Z2 HHS CZ |i⟩
72-74 Z1 HHS CZ X2 Z2 |i⟩
75-77 X2 Z2 Z1 HHS CZ |i⟩
78-80 HHS X2 Z2 CZ CZ |i⟩
81-83 X1 X2 X1 X2 X1 |i⟩
84-86 Z2 Z1 X1 Z2 CZ |i⟩
87-89 HHS CZ HHS X2 CZ |i⟩
90-92 Z2 CZ X2 X2 X1 Z1 |i⟩
93-95 Z1 X2 Z1 X2 X1 Z1 |i⟩
96-98 Z1 Z2 X1 Z1 HHS X2 |i⟩
99-101 Z2 CZ X1 HHS X1 CZ |i⟩
102-104 X2 CZ HHS X2 CZ Z2 |i⟩
105-107 X1 X1 X1 X2 X2 Z2 |i⟩
108-110 Z1 X2 Z2 CZ X2 X1 X1 |i⟩
111-113 HHS X2 X2 Z2 Z2 X1 X1 |i⟩
114-116 Z2 X1 Z2 X2 CZ HHS CZ |i⟩
117-119 X2 Z2 Z1 HHS Z1 HHS HHS |i⟩
120-122 CZ Z2 Z1 Z2 X1 CZ X2 |i⟩
123-125 X2 HHS Z1 X1 X2 CZ X2 |i⟩
126-128 Z2 Z1 HHS HHS X2 X1 Z2 CZ |i⟩
129-131 Z1 X2 Z1 HHS CZ Z2 Z2 X2 |i⟩
132-134 CZ Z2 HHS Z2 HHS CZ Z2 HHS |i⟩
135-137 CZ X2 CZ CZ X2 X2 Z2 Z2 |i⟩
138-140 Z1 Z2 CZ CZ X1 X1 X2 X2 |i⟩
141-143 HHS X1 X2 X1 X2 Z2 Z1 X1 |i⟩
144-146 HHS CZ X2 HHS X1 X1 Z1 X1 X2 |i⟩
147-149 X1 X1 HHS Z2 HHS HHS X2 Z2 CZ |i⟩
150-152 X1 CZ HHS CZ HHS Z1 CZ CZ X2 |i⟩
153-155 CZ X1 Z2 HHS X2 X1 Z1 Z1 HHS |i⟩
156-158 X2 CZ HHS HHS HHS Z2 CZ CZ Z1 |i⟩
159-161 Z2 HHS CZ X2 X2 Z1 Z2 X1 X1 |i⟩
162-164 X2 X1 CZ HHS CZ Z1 Z1 X1 X2 Z2 |i⟩
165-167 Z2 X1 Z1 Z1 CZ Z1 X2 Z1 HHS CZ |i⟩
168-170 CZ HHS X1 Z2 X2 X2 X2 Z2 HHS CZ |i⟩
171-173 CZ X1 X2 Z1 Z1 X1 X1 Z1 Z1 Z2 |i⟩
174-176 Z2 Z2 Z2 X2 Z1 CZ CZ Z2 X2 X2 |i⟩
177-179 Z1 X2 HHS CZ X1 HHS CZ CZ X1 X1 |i⟩
180-182 Z2 Z2 |i⟩
183-185 Z2 Z2 Z2 |i⟩
186-188 Z2 Z2 Z2 Z2 |i⟩
189-191 Z2 Z2 Z2 Z2 Z2 |i⟩
192-194 Z2 Z2 Z2 Z2 Z2 Z2 |i⟩
195-197 Z2 Z2 Z2 Z2 Z2 Z2 Z2 |i⟩
198-200 Z2 Z2 Z2 Z2 Z2 Z2 Z2 Z2 |i⟩
201-203 Z2 Z2 Z2 Z2 Z2 Z2 Z2 Z2 Z2 |i⟩
204-206 Z2 Z2 Z2 Z2 Z2 Z2 Z2 Z2 Z2 Z2 |i⟩
207-209 CZ CZ |i⟩
210-212 CZ CZ CZ |i⟩
213-215 CZ CZ CZ CZ |i⟩
216-218 CZ CZ CZ CZ CZ |i⟩
219-221 CZ CZ CZ CZ CZ CZ |i⟩
222-224 CZ CZ CZ CZ CZ CZ CZ |i⟩
225-227 CZ CZ CZ CZ CZ CZ CZ CZ |i⟩
228-230 CZ CZ CZ CZ CZ CZ CZ CZ CZ |i⟩
231-233 CZ CZ CZ CZ CZ CZ CZ CZ CZ CZ |i⟩
234-236 X1 X1 |i⟩
237-239 X1 X1 X1 X1 |i⟩
240-242 X1 X1 X1 X1 X1 |i⟩
243-245 X1 X1 X1 X1 X1 X1 |i⟩
246-248 X1 X1 X1 X1 X1 X1 X1 |i⟩
249-251 X1 X1 X1 X1 X1 X1 X1 X1 |i⟩
252-254 X1 X1 X1 X1 X1 X1 X1 X1 X1 |i⟩
255-257 X1 X1 X1 X1 X1 X1 X1 X1 X1 X1 |i⟩
258-260 HHS CZ |i⟩
261-263 HHS CZ HHS CZ |i⟩
264-266 HHS CZ HHS CZ HHS CZ |i⟩
267-269 HHS CZ HHS CZ HHS CZ HHS CZ |i⟩
270-272 HHS CZ HHS CZ HHS CZ HHS CZ HHS CZ |i⟩
273-275 Z1 Z2 Z1 Z2 |i⟩
276-278 Z1 Z2 Z1 Z2 Z1 Z2 |i⟩
279-281 Z1 Z2 Z1 Z2 Z1 Z2 Z1 Z2 |i⟩
282-284 Z1 Z2 Z1 Z2 Z1 Z2 Z1 Z2 Z1 Z2 |i⟩
285-287 X2 X2 |i⟩
288-290 X2 X2 X2 X2 |i⟩
291-293 X2 X2 X2 X2 X2 X2 |i⟩
294-296 X2 X2 X2 X2 X2 X2 X2 X2 |i⟩
297-299 X2 X2 X2 X2 X2 X2 X2 X2 X2 X2 |i⟩
300-302 X2 Z1 X2 Z1 |i⟩
303-305 X2 Z1 X2 Z1 X2 Z1 |i⟩
306-308 X2 Z1 X2 Z1 X2 Z1 X2 Z1 |i⟩
309-311 X2 Z1 X2 Z1 X2 Z1 X2 Z1 X2 Z1 |i⟩
312-314 X1 HHS X1 HHS |i⟩
315-317 X1 HHS X1 HHS X1 HHS |i⟩
318-320 X1 HHS X1 HHS X1 HHS X1 HHS |i⟩
321-323 X1 HHS X1 HHS X1 HHS X1 HHS X1 HHS |i⟩
324-326 Z2 Z1 |i⟩
327-329 Z2 Z1 Z2 Z1 |i⟩
330-332 Z2 Z1 Z2 Z1 Z2 Z1 |i⟩
333-335 Z2 Z1 Z2 Z1 Z2 Z1 Z2 Z1 |i⟩
336-338 Z2 Z1 Z2 Z1 Z2 Z1 Z2 Z1 Z2 Z1 |i⟩
339-341 CZ CZ X1 |i⟩
342-344 CZ CZ X1 CZ CZ X1 |i⟩
345-347 CZ CZ X1 CZ CZ X1 CZ CZ X1 |i⟩
348-350 X1 CZ Z2 |i⟩
351-353 X1 CZ Z2 X1 CZ Z2 |i⟩
354-356 X1 CZ Z2 X1 CZ Z2 X1 CZ Z2 |i⟩
357-359 CZ CZ X2 |i⟩
360-362 CZ CZ X2 CZ CZ X2 |i⟩
363-365 CZ CZ X2 CZ CZ X2 CZ CZ X2 |i⟩
366-368 Z1 Z1 X1 |i⟩
369-371 Z1 Z1 X1 Z1 Z1 X1 |i⟩
372-374 Z1 Z1 X1 Z1 Z1 X1 Z1 Z1 X1 |i⟩
375-377 X2 Z2 HHS |i⟩
378-380 X2 Z2 HHS X2 Z2 HHS |i⟩
381-383 X2 Z2 HHS X2 Z2 HHS X2 Z2 HHS |i⟩
384-386 HHS HHS X2 |i⟩
387-389 HHS HHS X2 HHS HHS X2 |i⟩
390-392 HHS HHS X2 HHS HHS X2 HHS HHS X2 |i⟩
393-395 HHS CZ X2 CZ |i⟩
396-398 HHS CZ X2 CZ HHS CZ X2 CZ |i⟩
399-401 Z1 HHS HHS X2 |i⟩
402-404 Z1 HHS HHS X2 Z1 HHS HHS X2 |i⟩
405-407 Z2 Z1 X2 Z2 |i⟩
408-410 Z2 Z1 X2 Z2 Z2 Z1 X2 Z2 |i⟩
411-413 Z2 X1 Z2 X2 |i⟩
414-416 Z2 X1 Z2 X2 Z2 X1 Z2 X2 |i⟩
417-419 Z1 Z1 X2 X2 |i⟩
420-422 Z1 Z1 X2 X2 Z1 Z1 X2 X2 |i⟩
423-425 X2 HHS Z2 Z2 |i⟩
426-428 X2 HHS Z2 Z2 X2 HHS Z2 Z2 |i⟩
429-431 Z1 Z2 Z1 HHS X1 |i⟩
432-434 Z1 Z2 Z1 HHS X1 Z1 Z2 Z1 HHS X1 |i⟩
435-437 Z1 CZ Z1 Z2 HHS |i⟩
438-440 Z1 CZ Z1 Z2 HHS Z1 CZ Z1 Z2 HHS |i⟩
441-443 Z1 Z2 X2 Z1 HHS |i⟩
444-446 Z1 Z2 X2 Z1 HHS Z1 Z2 X2 Z1 HHS |i⟩
447-449 X1 Z2 HHS CZ CZ |i⟩
450-452 X1 Z2 HHS CZ CZ X1 Z2 HHS CZ CZ |i⟩
453-455 X1 X1 X1 HHS Z2 |i⟩
456-458 X1 X1 X1 HHS Z2 X1 X1 X1 HHS Z2 |i⟩
459-461 HHS X1 Z2 X1 Z2 |i⟩
462-464 HHS X1 Z2 X1 Z2 HHS X1 Z2 X1 Z2 |i⟩

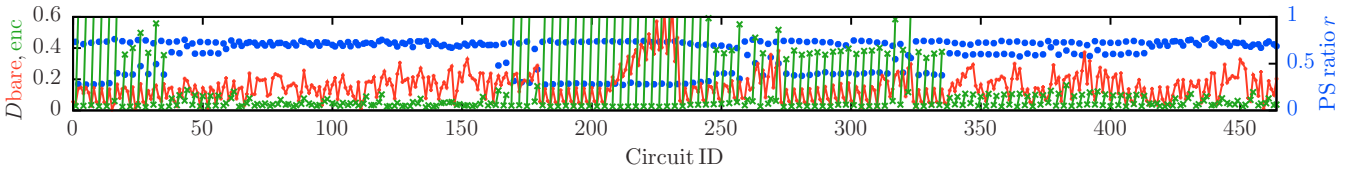

FIG. 7. Test of the fault-tolerance criterion in system (3) (see Sec. V) for all 465 circuits using the qubits (Q_4, Q_3, Q_2, Q_{15}, Q_{14}) of the IBM 16-qubit device `ibmqx5` on April 20, 2018. Shown are the statistical distances to the ideal result for the selected bare (red plusses) and encoded (green crosses) circuits, and the postselection ratios (blue dots). All plotted quantities are dimensionless. Only the circuits that could be mapped on the topology were run on the real device. Lines connecting the data points are guides to the eye.

APPENDIX C: SPECIFICATION OF THE SIMULATION MODELS

1. Spin qubits coupled to an environment

The model of five spin qubits coupled to an environment with N_E two-level defects is defined by the Hamiltonian given in Eqs. (4)–(7). For this Hamiltonian, we numerically solve the TDSE given in Eq. (1) by means of the Chebyshev polynomial algorithm to machine precision [42,43,51], which yields the state $|\Psi(t)\rangle$ of the system after execution of a particular circuit.

By construction, the only source of errors in this model is the interaction of the qubits with the environment controlled by the coupling strength λ. For $\lambda = 0$, the quantum computer model is designed to work perfectly. Therefore, the quantum gates in this model are not implemented by pulses, but by choosing suitable parameters h_n^α and G_{nm}^α for H_Q given by Eq. (5) [51], and having the system evolve through the TDSE given in Eq. (1) for a certain time t. The specific set of parameters for the gates used in the tested circuits is given in Table VI. The two-qubit gate CNOT_{nm} between qubits n and m is implemented through the gate sequence $H_n I_{nm} H_n$, where H_n is the Hadamard gate on qubit n and I_{nm} implements a two-qubit evolution of the form $\sigma_n^x + \sigma_m^x - \sigma_n^x \sigma_m^x$ through Eq. (5) (see Table VI).

In addition to the results for $\lambda \in [0.01, 0.2]$ presented in Sec. III, we have studied the performance of the circuits for various numbers N_E of two-level systems in the environment (see Fig. 9) and various inverse temperatures β (see Fig. 10).

The number N_E of two-level systems in the environment is limited by two factors. On the one hand, it should not be too small for decoherence effects to be observable, so $N_E = 5$ is the smallest case that we consider. In this case, the virtual interaction between two spin qubits mediated by the environment has a significantly smaller path than for larger N_E, so the influence of the environment on the performance is rather strong [see Fig. 9(a)]. On the other hand, there is a practical limitation given by the available computational resources on the supercomputer. For $N_E = 27$, the dimension of the total Hilbert space is 2^{32}, so the simulation of the full time evolution is rather expensive. Hence, this is the bound we set for what can be simulated with a reasonable amount of computer resources (CPU time and memory). By comparing the results for $N_E = 20$ to those for $N_E = 27$, shown in Figs. 9(b) and 9(c), respectively, we find that there is no significant qualitative change. In particular, the statistical distances D_{enc} for the encoded circuits all lie between 0 and 0.15, with only small fluctuations between the results for $N_E = 20$ and $N_E = 27$. But the main observation is that in all cases, some circuits perform better when they are encoded, while others are better without encoding.

The dependence of the fault-tolerance test on the inverse temperature β is shown in Fig. 10. We find no significant difference between the results for $\beta = 0$ and $\beta = 1$ shown in Figs. 10(a) and 10(b), respectively. These cases represent the high-temperature regime. In contrast, the results for $\beta = 5$, shown in Fig. 10(c), resemble the results from the smallest environment $N_E = 5$, shown in Fig. 9(a). Hence, this low-temperature regime indicates that the system is no longer affected by pure decoherence, but that other effects also come into play. However, although some influence of the temperature on the performance of the circuits can be observed, the qualitative results do not change. This means that the bare circuits that outperform their encoded equivalents are the same in each case. Hence, in this system, the criterion for fault tolerance is not satisfied in any of the regimes under investigation.

2. Transmon simulation

The Hamiltonian given in Eqs. (8)–(10) models five transmon qubits coupled by six resonators, as schematically shown in Fig. 3. The full set of relevant device parameters is

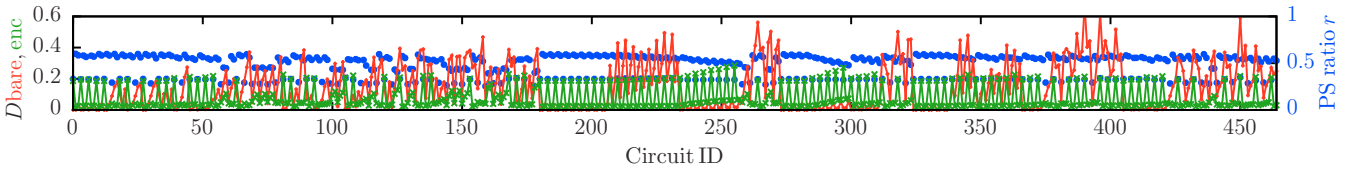

FIG. 8. Test of the fault-tolerance criterion in the decoherence model [system (1), see Sec. III] using $N_E = 5$, $\beta = 1$, and $\lambda = 0.1$ for the full set of circuits. Shown are the statistical distances to the ideal result for the selected bare (red plusses) and encoded (green crosses) circuits, and the postselection ratios (blue dots). All plotted quantities are dimensionless. Lines connecting the data points are guides to the eye.

TABLE VI. Summary of the parameters for the required set of quantum gates [see Eqs. (A7)–(A12)], implemented through the time evolution of H_Q given in Eq. (5). Each parameter h_n^α and G_{nm}^α is given in GHz, and the duration t of the corresponding gate is given in ns.

Gate	h_n^x	h_m^x	h_n^z	G_{nm}^x	t
X_n	1		0	0	$\pi/2$
Z_n	0		$15+n/2$	0	$\pi/(30+n)$
S_n	0		$15+n/2$	0	$\pi/(60+2n)$
H_n	$15+n/2$		$15+n/2$	0	$\pi/\sqrt{2}/(30+n)$
I_{nm}	-0.025	-0.025	0	0.025	10π

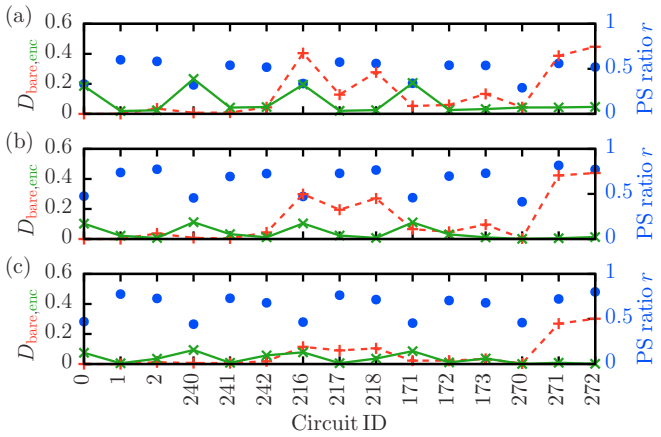

FIG. 9. Test of the fault-tolerance criterion for different environment sizes (a) $N_E = 5$, (b) $N_E = 20$, and (c) $N_E = 27$. Shown are the statistical distances to the ideal result for the selected bare (dashed red line) and encoded (solid green line) circuits, and the postselection ratios (blue dots). All plotted quantities are dimensionless. The simulations were done for inverse temperature $\beta = 1$ and coupling strength $\lambda = 0.1$. Lines connecting the data points are guides to the eye.

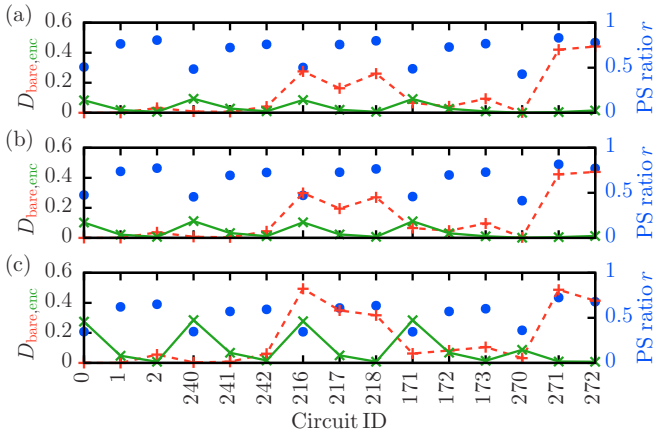

FIG. 10. Test of the fault-tolerance criterion for different inverse temperatures (a) $\beta = 0$, (b) $\beta = 1$, and (c) $\beta = 5$. Shown are the statistical distances to the ideal result for the selected bare (dashed red line) and encoded (solid green line) circuits, and the postselection ratios (blue dots). All plotted quantities are dimensionless. All simulations were done for environment size $N_E = 20$ and coupling strength $\lambda = 0.1$. Lines connecting the data points are guides to the eye.

TABLE VII. Device parameters of the transmon Hamiltonian defined in Eq. (9). All values are given in GHz. The charging energies E_C and the Josephson energies E_J define the transmon qubits. The qubit frequencies ω have been obtained by preparing the respective qubit in the state $|+\rangle$ and all other qubits in the state $|0\rangle$, having the entire system evolve for 1000 ns, and measuring the frequency of $\langle\sigma^x(t)\rangle$. The drive frequencies ω^{dr} result from additionally tuning this ω in the single-qubit pulse-optimization procedure. These frequencies are only used by the gate set labeled `*-withf`.

	q_0	q_1	q_2	q_3	q_4
$E_C/2\pi$	0.301	0.301	0.301	0.301	0.301
$E_J/2\pi$	11.6671	12.1273	13.003	12.2456	11.1943
$\omega/2\pi$	4.97154	5.07063	5.26657	5.10145	4.86036
$\omega^{\text{dr}}/2\pi$	4.97164	5.07043	5.26634	5.10147	4.86055

summarized in Table VII and Table VIII. We numerically solve the TDSE in Eq. (1) for the time-dependent Hamiltonian given in Eq. (8), using the unconditionally stable Suzuki-Trotter product-formula algorithm [50,51] to second order, to obtain $|\Psi(t)\rangle$ at any time t. In this work, we express the full state $|\Psi(t)\rangle$ in the joint eigenbasis of the five transmons and the six resonators $|m_0\cdots m_4; k_0\cdots k_5\rangle$, where each transmon index m_i enumerates the first four eigenstates of $4E_{Ci}\hat{n}_i^2 - E_{Ji}\cos\hat{\varphi}_i$, and the resonator indices k_r enumerate the first four Fock states. The algorithm results in four-component updates of the full state $|\Psi(t)\rangle$ at each time step $\tau = 0.001$ ns. We have verified that this basis accurately covers the system dynamics by comparison with exact diagonalization and with the simulation in the charge basis (see [5] where 17 levels were included for each transmon).

Quantum gates are implemented by choosing a particular pulse for $n_{gi}(t)$ in the time-dependent Hamiltonian given in Eq. (9). As in the corresponding experiments [52,56], a single-qubit pulse on qubit i is defined by

$$n_{gi}(t) = \Omega_{\text{G}}(t)\cos(2\pi f t - \gamma) + \beta_X\dot{\Omega}_{\text{G}}(t)\cos\left(2\pi f t - \gamma - \frac{\pi}{2}\right), \tag{C1}$$

where $\Omega_{\text{G}}(t)$ is a Gaussian with amplitude Ω_X, duration $T_X = 80$ ns, and width $\sigma = T_X/4$ (see [5]), β_X is the DRAG coefficient [53,57], f is the drive frequency, and γ is a phase parameter used to implement VZ gates [52]. The two-qubit CNOT gate is implemented using an echoed cross-resonance scheme [5,47,56], in which the single-qubit pulses implementing the echo are realized by Eq. (C1), and the flat-top Gaussians are

TABLE VIII. Device parameters of the resonator Hamiltonian defined in Eq. (10). All values are given in GHz.

	r_0	r_1	r_2	r_3	r_4	r_5
$\Omega/2\pi$	6.45	6.25	6.65	6.65	6.45	6.85
$G/2\pi$	0.07	0.07	0.07	0.07	0.07	0.07
Coupled to	q_1, q_2	q_0, q_1	q_2, q_3	q_1, q_4	q_3, q_4	q_0, q_4

TABLE IX. Parameters of the Gaussian `xpih-*` pulses defined by Eq. (C1). The drive frequencies f are given in GHz and the pulse time T_X and the DRAG coefficient β_X are given in ns. The Gaussian drive amplitudes Ω_X are unitless. All pulses labeled `*-withf` represent pulses with frequency tuning, meaning that the drive frequency has additionally been optimized in the pulse-optimization procedure.

Pulse name	f	T_X	Ω_X	β_X
`xpih-0`	4.97154	80	0.00238	1.335
`xpih-1`	5.07063	80	0.00236	−1.904
`xpih-2`	5.26657	80	0.00233	−2.165
`xpih-3`	5.10145	80	0.00236	0.498
`xpih-4`	4.86036	80	0.00241	2.276
`xpih-0-withf`	4.97164	80	0.00239	0.239
`xpih-1-withf`	5.07043	80	0.00236	0.238
`xpih-2-withf`	5.26634	80	0.00233	0.229
`xpih-3-withf`	5.10147	80	0.00236	0.232
`xpih-4-withf`	4.86055	80	0.00241	0.236

obtained from the same equation by choosing $\beta_X = 0$ and $\Omega_G(t)$ to rise for $0 \leqslant t \leqslant 15\,\text{ns}$ with $\sigma = 5\,\text{ns}$, stay constant at Ω_{CR} for $15 < t < 15\,\text{ns} + T_{\text{CR}}$, and fall again for $15 + T_{\text{CR}} \leqslant t \leqslant 30\,\text{ns} + T_{\text{CR}}$ (see [5] for more information).

We optimize two sets of gate pulses for the experiments, namely, one without frequency tuning and one with frequency tuning. The pulses without frequency tuning use the qubit frequencies as drive frequencies, i.e., $f = \omega/2\pi$, where the qubit frequencies ω are taken from Table VII. In contrast, with frequency tuning, the pulse-optimization procedure also fits the drive frequencies, such that the resulting pulses have the drive frequencies $f = \omega^{\text{dr}}/2\pi$ (the corresponding values are also listed in Table VII). To distinguish between both gate sets, we attach the suffix `-withf` to the pulses with frequency tuning. The relevant parameters resulting from a Nelder-Mead optimization [58] are summarized in Table IX and Table X.

TABLE XI. Gate metrics resulting from the pulse-optimization procedure. Δ is the distance objective (loss function), $\eta_\diamond$ is the diamond distance, F_{avg} is the average gate fidelity, and u is the unitarity (see [5] for more information about these metrics).

Pulse name	Δ	$\eta_\diamond$	F_{avg}	u
`xpih-0`	4.60×10^{-5}	0.007	0.9930	0.9860
`xpih-1`	1.19×10^{-4}	0.011	0.9884	0.9770
`xpih-2`	7.52×10^{-6}	0.002	0.9962	0.9925
`xpih-3`	8.99×10^{-6}	0.003	0.9965	0.9930
`xpih-4`	4.17×10^{-5}	0.006	0.9934	0.9868
`xpih-0-withf`	4.59×10^{-5}	0.007	0.9930	0.9860
`xpih-1-withf`	1.14×10^{-4}	0.011	0.9887	0.9774
`xpih-2-withf`	7.20×10^{-6}	0.002	0.9963	0.9927
`xpih-3-withf`	8.85×10^{-6}	0.003	0.9965	0.9930
`xpih-4-withf`	3.87×10^{-5}	0.006	0.9936	0.9873
`cnot-1-0`	1.34×10^{-2}	0.071	0.9852	0.9758
`cnot-1-4`	1.08×10^{-1}	0.177	0.9621	0.9668
`cnot-2-1`	4.68×10^{-2}	0.119	0.9714	0.9615
`cnot-3-2`	1.83×10^{-2}	0.088	0.9852	0.9777
`cnot-3-4`	9.54×10^{-2}	0.179	0.9671	0.9720
`cnot-4-0`	2.78×10^{-1}	0.284	0.9347	0.9783
`cnot-1-0-withf`	5.70×10^{-2}	0.149	0.9751	0.9728
`cnot-1-4-withf`	7.13×10^{-3}	0.056	0.9841	0.9712
`cnot-2-1-withf`	1.38×10^{-2}	0.081	0.9806	0.9668
`cnot-3-2-withf`	1.21×10^{-1}	0.207	0.9644	0.9764
`cnot-3-4-withf`	1.88×10^{-2}	0.090	0.9832	0.9740
`cnot-4-0-withf`	8.27×10^{-2}	0.168	0.9739	0.9806

For each pulse, we evaluate various gate metrics such as the matrix distance Δ used as the objective function in the optimization [5], the diamond distance $\eta_\diamond$ [35], the average gate fidelity F_{avg} [59], and the unitarity u [60]. These metrics are reported in Table XI.

TABLE X. Parameters defining the echoed cross-resonance pulses (CR2 in [5]) to implement the CNOT gate. The drive frequencies f_C and f_T are given in GHz. The times T_{CR} of the flat top in a cross-resonance pulse, the Gaussian pulse times T_X, and the DRAG coefficients β_C and β_T are given in ns. The Gaussian drive amplitudes Ω_{CR} and Ω_C on the control qubit and Ω_T on the target qubit are unitless. All pulses labeled `*-withf` represent pulses with frequency tuning, meaning that the drive frequency has also been optimized in the pulse-optimization procedure.

Pulse name	f_C	f_T	T_{CR}	T_X	Ω_{CR}	Ω_C	β_C	Ω_T	β_T
`cnot-1-0`	5.07063	4.97154	76.955	80	0.0097	0.00461	0.640	0.00238	1.335
`cnot-1-4`	5.07063	4.86036	64.161	80	0.0183	0.00476	−0.148	0.00241	2.276
`cnot-2-1`	5.26657	5.07063	33.398	80	0.0235	0.00465	−0.036	0.00236	−1.904
`cnot-3-2`	5.10145	5.26657	242.064	80	0.0111	0.00471	0.508	0.00233	−2.165
`cnot-3-4`	5.10145	4.86036	33.247	80	0.0290	0.00465	0.640	0.00241	2.276
`cnot-4-0`	4.86036	4.97154	105.151	80	0.0210	0.00449	−1.511	0.00238	1.335
`cnot-1-0-withf`	5.07043	4.97164	73.538	80	0.0101	0.00477	0.798	0.00239	0.239
`cnot-1-4-withf`	5.07043	4.86055	109.439	80	0.0114	0.00472	0.502	0.00241	0.236
`cnot-2-1-withf`	5.26634	5.07043	82.077	80	0.0111	0.00463	0.661	0.00236	0.238
`cnot-3-2-withf`	5.10147	5.26634	58.763	80	0.0429	0.00480	−0.198	0.00233	0.229
`cnot-3-4-withf`	5.10147	4.86055	85.294	80	0.0118	0.00474	0.247	0.00241	0.236
`cnot-4-0-withf`	4.86055	4.97164	98.599	80	0.0239	0.00483	0.115	0.00239	0.239

[1] S. Sheldon, L. S. Bishop, E. Magesan, S. Filipp, J. M. Chow, and J. M. Gambetta, Phys. Rev. A **93**, 012301 (2016).

[2] J. M. Gambetta, J. M. Chow, and M. Steffen, npj Quantum Inf. **3**, 2 (2017).

[3] C. Neill, P. Roushan, K. Kechedzhi, S. Boixo, S. V. Isakov, V. Smelyanskiy, A. Megrant, B. Chiaro, A. Dunsworth, K. Arya, R. Barends, B. Burkett, Y. Chen, Z. Chen, A. Fowler, B. Foxen, M. Giustina, R. Graff, E. Jeffrey, T. Huang, J. Kelly, P. Klimov, E. Lucero, J. Mutus, M. Neeley, C. Quintana, D. Sank, A. Vainsencher, J. Wenner, T. C. White, H. Neven, and J. M. Martinis, Science **360**, 195 (2018).

[4] IBM, Quantum experience, https://www.research.ibm.com/ibm-q/.

[5] D. Willsch, M. Nocon, F. Jin, H. De Raedt, and K. Michielsen, Phys. Rev. A **96**, 062302 (2017).

[6] K. Michielsen, M. Nocon, D. Willsch, F. Jin, Th. Lippert, and H. De Raedt, Comput. Phys. Commun. **220**, 44 (2017).

[7] P. W. Shor, *Proceedings of 37th Conference on Foundations of Computer Science, Burlington, VT* (IEEE, New York, 1996), pp. 56–65.

[8] D. Gottesman, Phys. Rev. A **57**, 127 (1998).

[9] E. T. Campbell, B. M. Terhal, and C. Vuillot, Nature (London) **549**, 172 (2017).

[10] M. Takita, A. D. Córcoles, E. Magesan, B. Abdo, M. Brink, A. Cross, J. M. Chow, and J. M. Gambetta, Phys. Rev. Lett. **117**, 210505 (2016).

[11] J. Kelly, R. Barends, A. G. Fowler, A. Megrant, E. Jeffrey, T. C. White, D. Sank, J. Y. Mutus, B. Campbell, Y. Chen, Z. Chen, B. Chiaro, A. Dunsworth, I.-C. Hoi, C. Neill, P. J. J. O'Malley, C. Quintana, P. Roushan, A. Vainsencher, J. Wenner, A. N. Cleland, and J. M. Martinis, Nature (London) **519**, 66 (2015).

[12] J. M. Chow, J. M. Gambetta, E. Magesan, D. W. Abraham, A. W. Cross, B. R. Johnson, N. A. Masluk, C. A. Ryan, J. A. Smolin, S. J. Srinivasan, and M. Steffen, Nat. Commun. **5**, 4015 (2014).

[13] A. Córcoles, E. Magesan, S. J. Srinivasan, A. W. Cross, M. Steffen, J. M. Gambetta, and J. M. Chow, Nat. Commun. **6**, 6979 (2015).

[14] D. Ristè, S. Poletto, M.-Z. Huang, A. Bruno, V. Vesterinen, O.-P. Saira, and L. DiCarlo, Nat. Commun. **6**, 6983 (2015).

[15] D. Gottesman, arXiv:1610.03507.

[16] D. W. Leung, M. A. Nielsen, I. L. Chuang, and Y. Yamamoto, Phys. Rev. A **56**, 2567 (1997).

[17] L. Vaidman, L. Goldenberg, and S. Wiesner, Phys. Rev. A **54**, R1745 (1996).

[18] M. Grassl, T. Beth, and T. Pellizzari, Phys. Rev. A **56**, 33 (1997).

[19] N. M. Linke, M. Gutierrez, K. A. Landsman, C. Figgatt, S. Debnath, K. R. Brown, and C. Monroe, Sci. Adv. **3**, e1701074 (2017).

[20] C. Vuillot, Quantum Inf. Comput. **18**, 0949 (2018).

[21] M. Takita, A. W. Cross, A. D. Córcoles, J. M. Chow, and J. M. Gambetta, Phys. Rev. Lett. **119**, 180501 (2017).

[22] R. Harper and S. Flammia, arXiv:1806.02359.

[23] F. Jin, H. De Raedt, S. Yuan, M. I. Katsnelson, S. Miyashita, and K. Michielsen, J. Phys. Soc. Jpn. **79**, 124005 (2010).

[24] P. Zhao, H. De Raedt, S. Miyashita, F. Jin, and K. Michielsen, Phys. Rev. E **94**, 022126 (2016).

[25] C. Müller, J. Lisenfeld, A. Shnirman, and S. Poletto, Phys. Rev. B **92**, 035442 (2015).

[26] E. Magesan, D. Puzzuoli, C. E. Granade, and D. G. Cory, Phys. Rev. A **87**, 012324 (2013).

[27] D. Puzzuoli, C. Granade, H. Haas, B. Criger, E. Magesan, and D. G. Cory, Phys. Rev. A **89**, 022306 (2014).

[28] P. S. Iyer and D. Poulin, Quantum Sci. Technol. **3**, 030504 (2018).

[29] M. A. Nielsen and I. L. Chuang, *Quantum Computation and Quantum Information: 10th Anniversary Edition* (Cambridge University Press, New York, 2011).

[30] B. M. Terhal and G. Burkard, Phys. Rev. A **71**, 012336 (2005).

[31] P. Aliferis, D. Gottesman, and J. Preskill, Quantum Inf. Comput. **6**, 97 (2006).

[32] P. Aliferis and B. M. Terhal, Quantum Inf. Comput. **7**, 139 (2007).

[33] D. Aharonov and M. Ben-Or, SIAM J. Comput. **38**, 1207 (2008).

[34] H. K. Ng and J. Preskill, Phys. Rev. A **79**, 032318 (2009).

[35] A. Y. Kitaev, Russ. Math. Surveys **52**, 1191 (1997).

[36] Y. R. Sanders, J. J. Wallman, and B. C. Sanders, New J. Phys. **18**, 012002 (2016).

[37] R. Kueng, D. M. Long, A. C. Doherty, and S. T. Flammia, Phys. Rev. Lett. **117**, 170502 (2016).

[38] T. Proctor, K. Rudinger, K. Young, M. Sarovar, and R. Blume-Kohout, Phys. Rev. Lett. **119**, 130502 (2017).

[39] R. Barends, J. Kelly, A. Megrant, D. Sank, E. Jeffrey, Y. Chen, Y. Yin, B. Chiaro, J. Mutus, C. Neill, P. O'Malley, P. Roushan, J. Wenner, T. C. White, A. N. Cleland, and J. M. Martinis, Phys. Rev. Lett. **111**, 080502 (2013).

[40] C. Wang, C. Axline, Y. Y. Gao, T. Brecht, Y. Chu, L. Frunzio, M. H. Devoret, and R. J. Schoelkopf, Appl. Phys. Lett. **107**, 162601 (2015).

[41] H. De Raedt, F. Jin, D. Willsch, M. Nocon, N. Yoshioka, N. Ito, S. Yuan, and K. Michielsen, arXiv:1805.04708.

[42] H. Tal-Ezer and R. Kosloff, J. Chem. Phys. **81**, 3967 (1984).

[43] V. V. Dobrovitski and H. A. De Raedt, Phys. Rev. E **67**, 056702 (2003).

[44] H. De Raedt, F. Jin, M. I. Katsnelson, and K. Michielsen, Phys. Rev. E **96**, 053306 (2017).

[45] A. Hams and H. De Raedt, Phys. Rev. E **62**, 4365 (2000).

[46] H. De Raedt, B. Barbara, S. Miyashita, K. Michielsen, S. Bertaina, and S. Gambarelli, Phys. Rev. B **85**, 014408 (2012).

[47] S. Sheldon, E. Magesan, J. M. Chow, and J. M. Gambetta, Phys. Rev. A **93**, 060302 (2016).

[48] J. Koch, T. M. Yu, J. Gambetta, A. A. Houck, D. I. Schuster, J. Majer, A. Blais, M. H. Devoret, S. M. Girvin, and R. J. Schoelkopf, Phys. Rev. A **76**, 042319 (2007).

[49] A. Blais, R.-S. Huang, A. Wallraff, S. M. Girvin, and R. J. Schoelkopf, Phys. Rev. A **69**, 062320 (2004).

[50] H. De Raedt, Comput. Phys. Rep. **7**, 1 (1987).

[51] H. De Raedt and K. Michielsen, in *Quantum and Molecular Computing, Quantum Simulations*, edited by M. Rieth and W. Schommers, Handbook of Theoretical and Computational Nanotechnology (American Scientific, Los Angeles, 2006), Vol. 3, pp. 1–48.

[52] D. C. McKay, C. J. Wood, S. Sheldon, J. M. Chow, and J. M. Gambetta, Phys. Rev. A **96**, 022330 (2017).

[53] J. M. Gambetta, F. Motzoi, S. T. Merkel, and F. K. Wilhelm, Phys. Rev. A **83**, 012308 (2011).

[54] J. M. Gambetta, A. D. Córcoles, S. T. Merkel, B. R. Johnson, J. A. Smolin, J. M. Chow, C. A. Ryan, C. Rigetti, S. Poletto, T. A. Ohki, M. B. Ketchen, and M. Steffen, Phys. Rev. Lett. **109**, 240504 (2012).

[55] M. Stephan and J. Doctor, J. Large-Scale Res. Facil. **1**, A1 (2015).

[56] J. M. Gambetta, in *Quantum Information Processing: Lecture Notes of the 44th IFF Spring School, Schriften des Forschungszentrums Jülich, Reihe Schlüsseltechnologien/Key Technologies*, edited by D. P. DiVincenzo (Forschungszentrum Jülich, Germany, 2013), Vol. 52.

[57] F. Motzoi, J. M. Gambetta, P. Rebentrost, and F. K. Wilhelm, Phys. Rev. Lett. **103**, 110501 (2009).

[58] J. A. Nelder and R. Mead, Comput. J. **7**, 308 (1965).

[59] M. A. Nielsen, Phys. Lett. A **303**, 249 (2002).

[60] J. Wallman, C. Granade, R. Harper, and S. T. Flammia, New J. Phys. **17**, 113020 (2015).